ORIGINAL RESEARCH ARTICLE

Effect of Variable Strain Rate on Hot Deformation Behavior of As-Extruded Mg-9Gd-4Y-1Zn-0.5Zr Alloy

Zhiwei Liang, Xiaobin Guo, Lingying Ye, Changping Tang, Yiping Wu, and Yunlai Deng

The hot deformation flow behavior and microstructure evolution of as-extruded Mg-9Gd-4Y-1Zn-0.5Zr alloy under constant and variable strain rates loading at 450 °C were investigated. It is interesting to find that there are two peak values of the flow stress and the maximum flow stress value is 142 MPa when compressed under the variable strain rate from $1 \ s^{-1}$ to $10 \ s^{-1}$, approaching the peak flow stress of 146 MPa under the constant strain rate condition with $1 \ s^{-1}$, but much smaller than that of 187 MPa under the constant strain rate condition with $10 \ s^{-1}$. Meanwhile, the area proportion of recrystallization grains is the largest but the grain orientation changes slightly under the variable strain rate condition. Analysis of microstructures and slip deformation effects on flow stress revealed that the subgrain dislocation density is the lowest under the variable strain rate, and the activation of pyramidal $<c + a>$ slip with the highest CRSS increases by 6%, contrasting with a 14% increase under the strain rate of constant $10 \ s^{-1}$. These findings indicate that the lower flow stress under the variable strain rate can be attributed to the reduced subgrain dislocation density and the limited activation of pyramidal $<c + a>$ slip systems.

Keywords	flow stress, isothermal compression, Mg-Gd-Y alloy, microstructure, variable strain rate

1. Introduction

Magnesium alloys become preferred materials to realize lightweight due to their excellent specific strength, which has great potential application in rail transportation, aerospace and other industrial fields (Ref 1-3). However, the relatively low absolute strength and poor plasticity hinder their application in structural materials (Ref 4). The reason for the poor plasticity is that few independent slip systems can be activated because of the hexagonal close-packed (HCP) structure (Ref 5), and its limited non-basal slip induces the activation of twin to adapt the plastic strain, resulting in poor formability through the plastic deformation process (Ref 6). What's more, a strong basal texture formed during basal slip will lead to the anisotropy of deformation (Ref 6). For the purpose of enhancing non-basal slip in magnesium alloys, rare earth (RE) elements were dissolved into the magnesium matrix which became one out of a multitude the most promising ways to achieve this goal (Ref 7).

To overcome the limitations of plasticity, RE elements such as Gd, Y, Nd and Ce were added to magnesium alloys and have developed magnesium rare earth (Mg-RE) alloys with excellent performances (Ref 8). Mg-RE alloys not only have excellent performance in terms of mechanical properties but also offer significant advantages in coupling anisotropy and improving strain rate sensitivity (SRS) (Ref 9), which have broadened the application scope of magnesium alloys. Over the last few years, Mg-Gd-Y-Zn-Zr alloys have gained widespread attention because of their excellent performance on mechanical properties and creep resistance (Ref 10-12). However, the high content of RE elements in magnesium alloy will affect the plasticity, which means a strong deformation resistance during the plastic processing (Ref 13). Thermomechanical processing methods, including temperature and strain rate, are often used to activate more slip systems to improve the formability of magnesium alloys. For Mg-RE alloys, the temperature of plastic deformation is usually above 300 °C and the optimum deformation temperature of as-extruded Mg-Gd-Y-Zn-Zr alloys is usually within a certain range of 380-450 °C (Ref 14). Strain rate, as another key parameter of deformation, has a great influence on deformation. There are multiple deformation modes exist in magnesium alloys under different loading paths and play different roles simultaneously. The SRSs of different deformation modes have large differences, with low sensitivity to strain rate in basal slip, while is high sensitivity in prismatic slip and pyramidal slip (Ref 8). The alloy has higher strength when deformed under high strain rates (Ref 15). In addition, deformation with high strain rates is favorable to increase the actual productivity and reduce costs. However, the risk of cracking increases because of the strong deformation resistance under high strain during manufacturing, so the formability of magnesium alloys under a strain rate greater than $1 \ s^{-1}$ is still challenging (Ref 16).

There are extensively reports regarding the hot deformation behavior of Mg-Gd-Y-Zn-Zr alloys (Ref 17-21), but most of the

Zhiwei Liang and Lingying Ye, School of Materials Science and Engineering, Central South University, Changsha 410083, China; Xiaobin Guo and Yunlai Deng, School of Materials Science and Engineering, Central South University, Changsha 410083, China; and Nation Key Laboratory of Science and Technology on High-Strength Structural Materials, Central South University, Changsha 410083, China; Changping Tang, School of Materials Science and Engineering, Hunan University of Science and Technology, Xiangtan 411201, China; and Yiping Wu, Department of Mechanical and Electrical Engineering, Changsha University, Changsha 410003, China. Contact e-mail: xiaobinguo@csu.edu.cn.

reports are studied under specific conditions that hold constant. However, in the actual thermomechanical processing, temperature and strain rate are continuously changing as the deformation proceeds. Although the contribution of deformation heat leads to a slowly change in temperature, the change of strain rate can reach an order of magnitude or even higher due to complex mold shapes (Ref 22). Some researchers (Ref 23-27) have reported studies in regard to the hot deformation behavior of different alloys with variable strain rates. Abbod et al. (Ref 23) used gradually changes in strain rate to investigate the effects of strain rate change between double deformations on flow stresses in plane strain compression experiments on 316L stainless steel. The flow stress principal equation was established by relating the stress to the instantaneous values of the Zener–Hollomon parameters, and this result indicated that the initial flow stress decreased due to the static recovery at the interrupted deformation with a strain of 0.25. The reduction of flow stress between the two deformations increases with time and Zener–Hollomon parameter. Liu et al. (Ref 24) looked into the microstructure and flow behavior of Inconel 718 during hot compression tests. It was found that there is a transient stage in which flow stress and the proportion of recrystallization variable gradually to the value that corresponds to constant strain rate under a variable strain rate. However, the duration of flow stress transient stage was inconsistent with that of recrystallization transient stage. The transient duration in flow stress was equal and larger than the transient duration in recrystallization for an abruptly increase in strain rate, whereas the transient duration of flow stress and recrystallization were exactly opposite for an abruptly decrease in strain rate. Zhang et al. (Ref 25) comparatively investigated the hot deformation behavior of C276 superalloy when compressed under a variable strain rate. The result indicated that flow stress changed immediately following the change in strain rate and it is beneficial to dynamic recrystallization when deformed from a high strain rate to a low strain rate. Chen et al. (Ref 26) researched the microstructure and flow behavior of Ni-based superalloy during compression under different strain rate conditions and showed that the proportion and average size of recrystallization grains have a positive correlation with temperature and negative correction with strain rate. Huang et al. (Ref 27) carried out hot compression experiments of 304L stainless steel under constant and variable strain rate conditions to analyze the hot deformation behavior of transient period. Results showed that before achieving the stage similar to deformed under a changeless strain rate, with the strain rate suddenly increased, the duration of transient stage was identical. Nevertheless, a smaller strain was required for flow stress and a bigger strain was required for substructure after the strain rate decreased.

However, there are limited researches that focus on the effect of a variable strain rate on the hot deformation behavior during two-stage deformation of magnesium alloys. In this work, isothermal compression experiments of Mg-9Gd-4Y-1Zn-05Zr as-extruded alloy under strain rates of constant $1\ \mathrm{s}^{-1}$ and $10\ \mathrm{s}^{-1}$ and suddenly changes from $1\ \mathrm{s}^{-1}$ to $10\ \mathrm{s}^{-1}$ at 450 °C were investigated to point out effects of the variable strain rate loading on the hot deformation flow behavior and microstructure evolution of Mg-9Gd-4Y-1Zn-0.5Zr alloys. Based on the analysis of recrystallization, grain orientation and dislocation density, the connection between flow stress and microstructure evolution will be revealed, which will provide guidance for the application of a variable strain rate loading to reduce the forming load of magnesium alloys.

2. Experimental Material and Methods

Commercial extrusion bar of WE94 magnesium alloy that ideal compositions of the alloy are Mg-9Gd-4Y-1Zn-0.5Zr (wt.%) was used as experimental material for isothermal compression in this work, and the diameter of the extrusion rod is 205 mm. The actual measured compositions of the purchased alloy are Mg-8.6Gd-4.1Y-1.2Zn-0.5Zr (wt.%), as listed in Table 1.

Compressed samples were processed by wire cutting parallel to the extrusion direction (ED). All samples have a diameter of 13 mm and a height of 20 mm which have an aspect ratio of height to diameter close to 1.5 to ensure stability during compression. Samples to be tested were placed on a Gleeble-3500 hot compression simulator and compressed at 450 °C with a cumulative reduction of 40% in the height direction. The experimental strain rates of uniaxial hot compression were set to constant $1\ \mathrm{s}^{-1}$, constant $10\ \mathrm{s}^{-1}$ and change from $1\ \mathrm{s}^{-1}$ to $10\ \mathrm{s}^{-1}$, termed as constant low strain rate, constant high strain rate and variable strain rate. The loading of constant strain rate means that the strain rate remains unchanged during hot compression testing, while variable strain rate loading means that the strain rate suddenly changes from $1\ \mathrm{s}^{-1}$ to $10\ \mathrm{s}^{-1}$ when sample height is reduced by 20% corresponding to a strain of 0.2, and two stages of variable strain rate compression are shown in Fig. 1(a). Before the compression deformation, the sample to be tested was preheated to a specified experimental temperature and kept for 200 s to make sure the internal temperature distribution was uniform. Once the specified strain of compression was reached, the microstructure was maintained by means of water quenching, and stress-strain data were obtained.

With the purpose of revealing the internal microstructure, samples after compressed were sectioned longitudinally along the central axis to facilitate the observation of the microstructure at the center of the section surface in the compression direction (CD), and the sampling and observation position are shown in Fig. 1(b). Before observation, the sample surface to be observed was bombarded with a Hitachi IM4000II planar argon ion polisher to remove the mechanical damage strain layer after pre-polishing with fine sandpaper. Thermo Scientific Apreo 2C field-emission gun SEM which is equipped with an EDAX Velocity Super EBSD detector was prepared to characterize microstructures of tested samples. The EBSD characterization test step size for all samples was 0.62 μm. The collected EBSD dataset was analyzed using the software of OIM Analysis 7 and Atex. For analysis of microstructures, the orientation angle of grain boundaries in the range of 2°and 15° is considered as low-angle grain boundaries (LAGBs), while the orientation angle of grain boundaries above 15° is considered as high-angle grain boundaries (HAGBs) (Ref 28, 29). The grain orientation spread (GOS) value between 0 and 2 is considered as recrystallization grains, and a value greater than 2 is defined as deformed grains (Ref 30, 31).

Table 1 Chemical composition of WE94 magnesium alloy (wt.%)

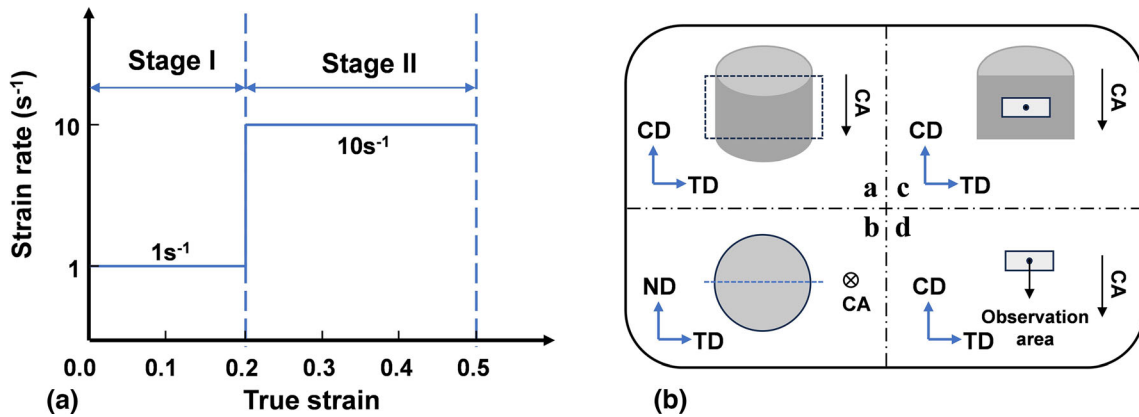| Elements	Gd	Y	Zn	Zr	Mg
Measured content	8.6	4.1	1.2	0.5	Bal.

Fig. 1 Isothermal compression of Mg-9Gd-4Y-1Zn-0.5Zr alloy. (a) Two stages of variable strain rate compression, (b) microstructure observation area of compression samples

3. Results

3.1 Flow Behavior during Hot Compression Testing

The experimental flow stress curves of Mg-9Gd-4Y-1Zn-0.5Zr alloy that deformed under strain rates of constant $1\ s^{-1}$, constant $10\ s^{-1}$ and change from $1\ s^{-1}$ to $10\ s^{-1}$ at 450 °C are displayed in Fig. 2. Black and red lines depict the deformation flow stress curves under strain rate of constant $1\ s^{-1}$ and $10\ s^{-1}$, while the blue line indicates that of under variable strain rate. It is obvious that flow stress sharply increases at the beginning of deformation, arriving at a maximum value of 146 MPa at a strain of ~ 0.04 under a strain rate of constant $1\ s^{-1}$ and 187 MPa at a strain of ~ 0.1 under another strain rate of constant $10\ s^{-1}$. Then, the flow stress gradually decreases as the strain continues to accumulate before obtaining the steady-state flow stress, and the steady-state flow varies between that under constant low strain rate and high strain rate. It is interesting to find out that two flow stress peaks have appeared during the variable strain rate compression and two flow stress peaks are extremely close. The first peak value of 142 MPa at a strain of ~ 0.06 is the compression under a constant low strain rate, while the second peak value of 139 MPa at a strain of ~ 0.26 is the maximum value when the constant low strain rate is accelerated to a higher strain rate. Compared with the constant high strain rate, the peak value of flow stress is greatly reduced when accelerating to a high strain rate during compression.

The experimental results show that flow stress curves rise rapidly at a small strain under different strain rates and then decreases slowly after attaining the maximum value at the given deformation conditions. Two stages are presented in flow stress curves, mainly caused by working hardening and dynamic recrystallization softening (Ref 32). For metals with high stacking fault energy (SFE), dynamic recovery is the common restoration mechanism. Although magnesium alloys have a high SFE and are not expected to occur dynamic recrystallization during hot deformation, it is prone to occur because of the operation of limited slip systems with HCP structure (Ref 33). In the first stage, a sharply elevated flow stress is exhibited on flow stress curves because of work hardening (Ref 34). When the alloy receives the compressive stress of loading, the internal dislocations multiply in large numbers and interact with each other to obstruct the movement of dislocations, increasing the deformation resistance and flow
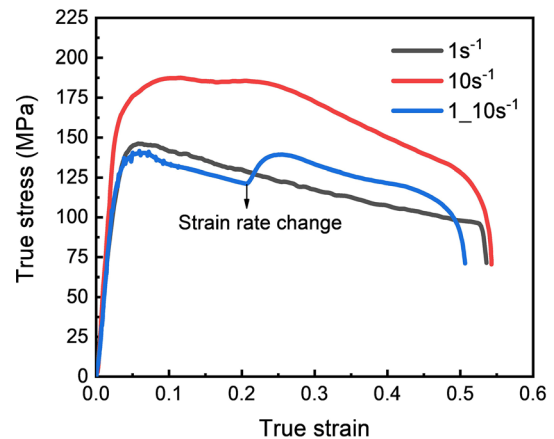

Fig. 2 Flow stress comparison of the alloy compressed under constant strain rate and variable strain rate

stress rapidly before reaching its peak value (Ref 35). After obtaining the peak value, dynamic recrystallization softening overtakes work hardening and becomes the main factor influencing flow stress in the second stage, and the flow stress curve shows a slowly decrease with the accumulation of strain (Ref 36) until arriving the steady state of dynamic equilibrium between work hardening and recrystallization softening (Ref 33).

3.2 Microstructure Characterization

Figure 3 and 4 shows the microstructure of the initial as-extruded Mg-9Gd-4Y-1Zn-0.5Zr alloy and the alloy after compressed under strain rates of constant $1\ s^{-1}$, constant $10\ s^{-1}$ and change from $1\ s^{-1}$ to $10\ s^{-1}$. There are different colors present in the grains, and different colors represent different orientations. It is observed in Fig. 3(a) that a variety of colors are randomly covered in fine grains and coarse grains are approximately a single red color. The initial as-extruded alloy consists of fibrous coarse deformed grains which elongated in the extrusion direction and a large number of fine recrystallization grains between deformed grain boundaries, exhibiting a bimodal grain structure distribution (Ref 37). After compression deformation, fibrous coarse deformed grains tend to be equiaxed due to flattening along the compression direction and the
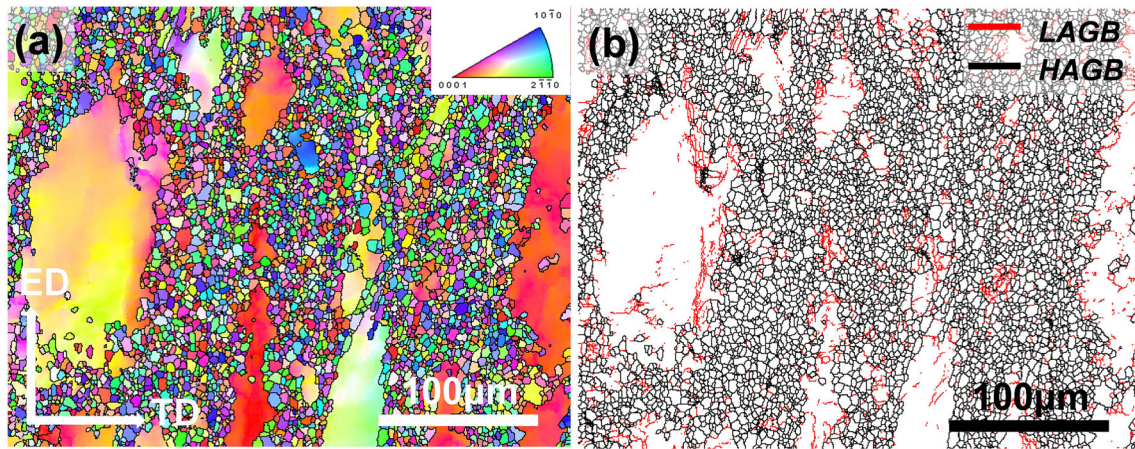
Fig. 3 Inverse pole figures and grain boundary maps of the initial as-extruded alloy

orientation of coarse grain which is reflected in the change of grain coloring changes obviously under different strain rate loading conditions. When deformed under the strain rate of constant 1 s^{-1}, a number of coarse grains are retained, as shown in Fig. 4(c). However, the orientation of some coarse grains is change, and both red and green colors are the dominant colors covered in coarse grains. When deformed under the strain rate of constant 10 s^{-1} and variable strain rate, the area proportion of recrystallization grains increases, while the number and size of coarse grains reduce dramatically, as shown in Fig. 4(a) and (e). The different is that orientation of coarse grains completely changes, and the color becomes a single green color under the strain rate of constant 10 s^{-1}, while orientation of coarse grains is almost consistent with the initial state and still remains a single red under the variable strain rate.

Figure 5 statistically presents the grain size of Mg-9Gd-4Y-1Zn-0.5Zr in different deformation states. As exhibited in Fig. 3, the distribution of grain size appears a clear bimodal feature and the maximum grain size is 113.79 μm with a 63.2% area proportion of recrystallization grains in the initial as-extruded alloy. After compression, changes in recrystallization area proportion and grain size are inconsistent. When compressed under strain rate of constant 1 s^{-1}, the area proportion of recrystallization grains is 60.1% with a maximum grain size of 94.42 μm, which are exhibited in Fig. 4(c), (d) and 5(c). When compressed under a strain rate of constant 10 s^{-1}, exhibited in Fig. 4(e), (f) and 5(d), the area proportion of recrystallization grains is 78.2% with the maximum grain size decreased to 66.38 μm. It is evident that coarse grains are gradually shrinking, masked by fine recrystallization grains, and the area proportion of recrystallization grains is moderately increasing with the strain rate increases when deformed under constant strain rates. When deformed under the variable strain rate, which is exhibited in Fig. 4(a), (b) and 5(b), the area proportion of recrystallization grains is 81.6%, the average size of grains is 3.13 μm, and the maximum grain size is 63.59 μm, with the smallest coarse grain size and the largest area proportion of recrystallization grains. From the above mentioned, the area proportion of recrystallization grains is largest under the variable strain rate, although it is comparable to the constant slow strain rate and lower than the constant high strain rate in terms of flow stress behavior.

During the hot deformation process, dynamic recrystallization grains nucleate at HAGBs, which occurs through the necklace mechanism. Dynamic recrystallization occurs when a first necklace layer is formed at the available boundary, followed by the formation of a new necklace layer at the boundary of the growth grain. The material will be fully recrystallized through the formation of subsequent necklace layers (Ref 33). Figure 3(b) and 4(b), (d), and (f) distinguishes the grain boundary distribution in different deformation states, where the red lines represent LAGBs and the black lines indicate HAGBs. It is obvious that LAGBs are mainly clustered around coarse grains, and the uniformly distributed fine equiaxed grain boundaries are HAGBs. LAGBs of the initial as-extruded alloy are mostly concentrated around coarse grain boundaries, and a very small number are scattered inside coarse grains. After compression, there are still more LAGBs that exist around the boundary of coarse grains, making coarse grains completely surrounded by LAGBs. However, after deformed under constant strain rate, basically all the coarse grains are surrounded by LAGBs, a large number of LAGBs with "chain-like" distribution appear inside the coarse grains from the edge to the inside, and the distribution of LAGBs is more concentrated under constant higher strain rate. After deformed under variable strain rate, except for extremely few coarse grains, the rest of coarse grains are basically covered by LAGBs, similar to the "net-like" distribution which reflects a fuller degree of recrystallization.

3.3 Textures and Schmid Factors

Figure 6 shows the whole grain {0001} pole figures of the initial alloy in extruded state and the alloy after compressed under different strain rates, as calculated according to the obtained EBSD data. It is evident that the overall texture intensity of the initial alloy is weak, but grains that are oriented near the center of the {0001} pole figure have a stronger relatively texture intensity with a maximum of 1.648. Moreover, the texture of initial alloy is parallel to the ED direction, exhibiting a representative feature of as-extruded alloys (Ref 38-40). This result is consistent with the coloring of coarse grains in IPF, illustrated in Fig. 3(a). The orientation of some grains distributed at both ends of the pole figure deviates from the ED direction and is closer to a random distribution with weak intensity, which mainly corresponds to fine recrystallized grains. It shows that the orientation of coarse grains in the bimodal grain structure has a great influence on the texture formation.
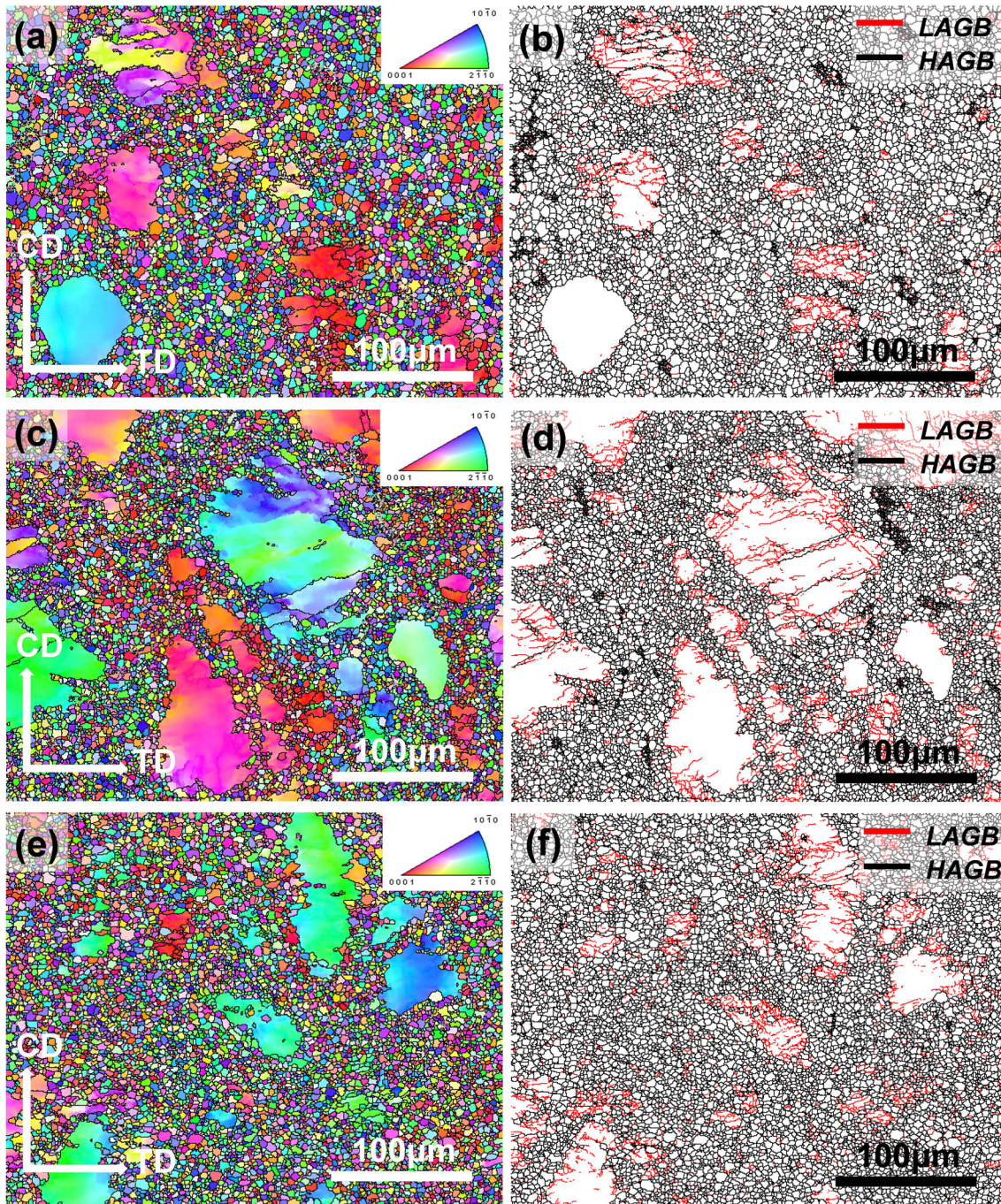
Fig. 4 Inverse pole figures and grain boundary maps of the alloy compressed under different strain rates. (a, b) Variable strain rate, (c, d) constant 1 s^{-1}, (e, f) constant 10 s^{-1}

After compression deformation, the overall texture intensity is slightly enhanced, it reached the maximum value of 2.007 under the strain rate of constant 1 s^{-1}, while reached the minimum value of 1.679 under the strain rate of constant 10 s^{-1}. The texture intensity of variable strain rate compression is between strain rate conditions of constant 1 s^{-1} and constant 10 s^{-1}, and much closer to the value under the strain rate of constant 1 s^{-1}. It is also clearly observed a change in the distribution of texture. As previously mentioned in section 3.2, the orientation of coarse grains completely changes under the constant high strain rate compared with the initial grain orientation, and the grain orientation partially changes

under the constant low strain rate with coarse grains exhibiting multiple orientations. However, the orientation of coarse grains changes only slightly under the variable strain rate. The texture is mainly distributed at both ends of the {0001} pole figure under strain rate of constant 10 s^{-1}, and these grains that initial orientation is gathered at the center of {0001} pole figure obviously rotate toward perpendicular to the CD direction. On the contrary, the majority of grain orientations remain clustered and distributed at the center of {0001} pole figure under the strain rate of constant 1 s^{-1} and variable strain rate, with maximum texture intensity of 2.007 and 1.996, respectively. What is not the same is that some grains of the
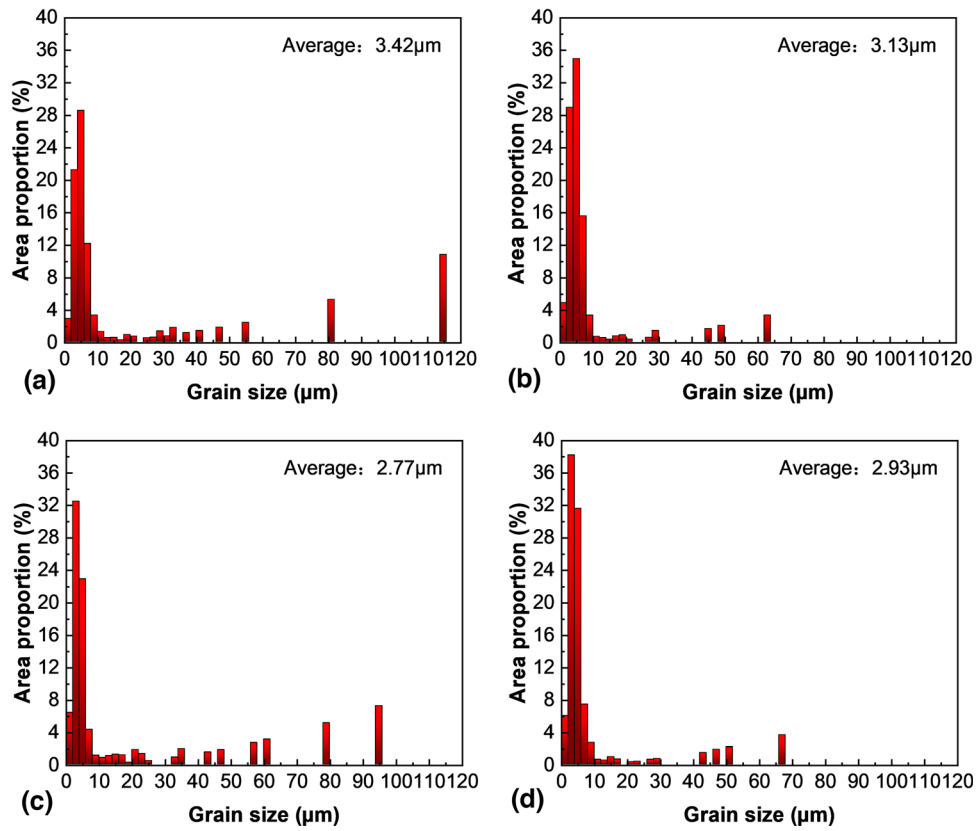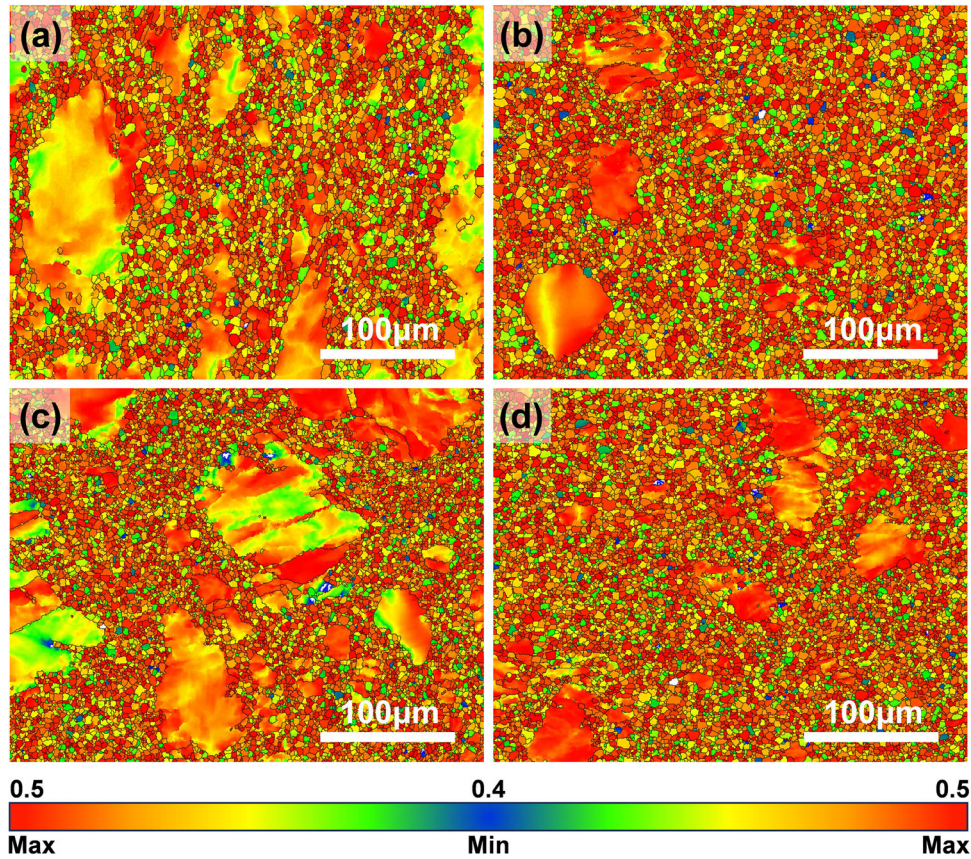
Fig. 5 Grain size distribution diagrams of the alloy under different conditions. (a) Initial, (b) variable strain rate, (c) constant 1 s^{-1}, (d) constant 10 s^{-1}
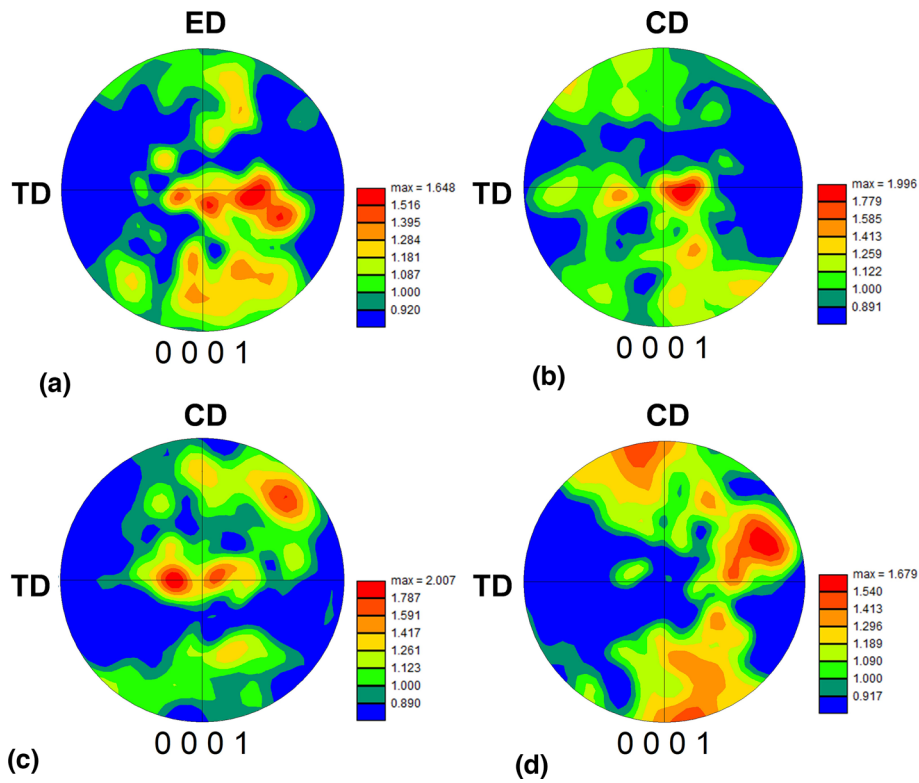
Fig. 6 {0001} pole figures of whole grains calculated from EBSD datasets. (a) Initial, (b) variable strain rate, (c) constant 1 s^{-1}, (d) constant 10 s^{-1}

Fig. 7 Schmid factor distribution of the alloy under different conditions. (a) Initial, (b) variable strain rate, (c) constant $1\ \mathrm{s}^{-1}$, (d) constant $10\ \mathrm{s}^{-1}$

initial alloy aggregated near the center of pole figure rotate toward perpendicular to CD direction and most grains orientation parallel to CD direction under the strain rate of constant $1\ \mathrm{s}^{-1}$, while under the variable strain rate, almost all grains are aggregated toward the center, maintaining a strong basal texture. Although the deformation of variable strain rate loading greatly reduces the size and area proportion of coarse grains, promoting the generation of fine recrystallization grains, it has no significant effect on the texture.

It also has a significant effect on slip deformation types when compressed under different strain rates. As Basal $<a>$ slip $\{0001\}\langle 11\bar{2}0\rangle$ with CRSS 28.0 MPa, Prismatic $<a>$ slip $\{10\bar{1}0\}\langle 11\bar{2}0\rangle$ with CRSS 67.7 MPa, Pyramidal $<a>$ slip $\{10\bar{1}1\}\langle 11\bar{2}0\rangle$ with CRSS 59.7 MPa, Pyramidal $<c+a>$ slip $\{\bar{1}\bar{1}22\}\langle 11\bar{2}3\rangle$ with CRSS 116.6 MPa are basic slip deformation types in magnesium alloy (Ref 41). Synthesize these four slip types and add the four slip types to a single map demonstrating the Schmid factors (SFs), as shown in Fig. 7.

The SF values for each grain of the as-extruded initial alloy and the alloy after compressive deformation under constant strain rate and variable strain rate are in the range of 0.4-0.5. The proportion of grains that SF values are bigger than 0.45 is 83.1%, 84.8%, 82.6% and 85.6%. The alloys after high strain rate and variable strain rate compression have bigger average SFs. However, activation of the slip deformation is decided by SFs and CRSS, the relationship between them can be used in Eq 1 according to Ref. [42] (Ref 42).

$$\sigma_{0.2} = \tau_{CRSS}/m \qquad\qquad (Eq\ 1)$$

where m is the SF, τ_{CRSS} is the CRSS—representing the critical value required for slip deformation mode activation. During slip deformation of magnesium alloys, the critical resolve shear stresses vary widely in different slip deformation modes, as mentioned above. As the CRSS values of basal slip, prismatic slip and pyramidal slip in magnesium alloys increase in order. From Eq 1, it can be seen that the increase in the SF values of slip systems with high CRSS or the more activation of slip systems with low CRSS at the same SF value is able to reduce the flow stress. For the purpose of analyzing this specifically, the proportion change of grains in slip systems within the same SF value will be discussed in section 4.2, which in turn explains the reason for the decrease in flow stress in the actual experimental results.

4. Discussion

During deformation under variable strain rate, flow stress curve indicates that the peak flow stress at the first stage that deformed under low strain rate is comparable to the peak value that deformed under constant low strain rate, while the peak flow stress is lower and reduced by more than 20% compared with the maximum value under constant high strain rate, at the second stage which deformed under a higher strain rate. In general, the flow behavior of hot deformation is connected with dislocation density, dynamic recrystallization, texture and slip (Ref 43-45). Therefore, the reasons for the reduction of the flow

stress caused by microstructure changes, including dislocation density and recrystallization, texture and slip will be discussed in follows.

4.1 Effect of Variable Strain Rate Compression on Microstructures

Previous studies (Ref 43) have shown that the link between flow stress and subgrains dislocation density under high temperature deformation is as follows:

$$\sigma = c_1 + c_2 Gb\rho_i^{1/2} \tag{Eq 2}$$

where ρ_i refers to the dislocation density, the c_1 and c_2 are constant, G refers to the modulus of rigidity, b refers to the Burgess vector, and they are also constant for a specific material. The change in dislocation density will cause a change in the flow stress. One of the reasons for the apparent differences in flow stress is the different homogeneous degrees of plastic deformation (Ref 46). This degree of homogenization can be reflected base on the Kernel Average Misorientation (KAM) density distribution. Figure 8 displays the KAM distribution of Mg-9Gd-4Y-1Zn-0.5Zr alloy under different strain rate conditions. The non-recrystallization grains show larger KAM values at LAGBs which are described in Fig. 3(b) and 4(b), Fig. 4(d) and (f), of which the recrystallization regions have smaller KAM values.

However, the KAM maps qualitatively give the local dislocation distribution and reflect the degree of plastic deformation and dislocation accumulation. Nevertheless, it is unable to give the detailed value of dislocation density, and the value of GND which represents geometrically necessary dislocation is able to quantitatively analyze the dislocation density of samples after deformation in a more intuitive way. The relationship between KAM and GND is shown in Eq 3 (Ref 47).

$$\rho_{\mathrm{GND}} = \frac{2\mathrm{KAM}_{\mathrm{ave}}}{\mu b} \tag{Eq 3}$$

where $\mathrm{KAM}_{\mathrm{ave}}$ is the average KAM values after compression under different strain rate conditions, μ is 0.62 μm in this work, indicating the scanning step of the EBSD tests, and b represents the Burgers vector of magnesium alloy, which is 0.32 according to Ref. [48] (Ref. 48).

In an attempt to distinguish the different influence between recrystallization grains and LAGBs (subgrains) on deformation, the average GND values of the whole grains and labeled positions in Fig. 8 were measured and counted after setting the values of μ and b in accordance with Eq 3 by combining with the Atex software, the square area represents the recrystallization grain regions, the circle area denotes the subgrain regions, and detailed values of dislocation density are listed in Table 2.

The flow stress during deformation is related to subgrains and recrystallization grains. Figure 9(a) exhibits the relation of peak flow stress and GND density. The recrystallization grain dislocation density is low, and the subgrain dislocation density is high under different strain rate conditions. Meanwhile, the recrystallization grain dislocation density is basically unchanged under different strain rates, while the subgrain dislocation density is the lowest under the variable strain rate and the highest under the high strain rate of constant 10 s^{-1}. According to Eq 2, it follows that subgrains with high

dislocation density have a more critical effect on the change of flow behavior during deformation. As described in section 3.2, the recrystallization area proportion is higher under the constant high strain rate compared with the constant low strain rate, while the recrystallization proportion is the largest under the variable strain rate. The recrystallization area proportion under the constant low strain rate is the smallest and slightly smaller than the initial alloy. Subgrains can be reflected by LAGB, with the largest LAGB proportion of 20.6% under the constant low strain rate despite having the lowest recrystallization area proportion, the second highest LAGB proportion of 15.9% under the constant high strain rate and the smallest LAGB proportion of 12.3% and the largest recrystallization area proportion of 81.6% under the variable strain rate, as shown in Fig. 9(b).

The dislocation density of subgrains offers storage energy for the nucleation and growth of recrystallization grains (Ref 49). The recrystallization nucleation must reach a critical value $\rho_m^3/\dot{\varepsilon}$, which is positively correlated with the cube of dislocation density and negatively correlated with strain rate. Table 2 shows the critical value of recrystallization nucleation under different deformation loading conditions. The dislocation proliferation is slow under the low strain rate of constant 1 s^{-1}, and the critical value of recrystallization nucleation is large, so the recrystallization nucleation is more difficult. The coarse grains are wrapped by dislocations gathered at grain boundaries, few dislocations are dispersed inside coarse grains, and the deformation is dominated by dynamic response at this time, so the size of coarse grains changes a little. Under the high strain rate of constant 10 s^{-1} and variable strain rate, it is relatively susceptible to dynamic recrystallization because of a small critical value of recrystallization nucleation. Moreover, during the process of deformation under variable strain rate, the critical value of recrystallization nucleation is the smallest, which is most conducive to dynamic recrystallization. The dislocation density gathered at the coarse grains is constantly consumed, with the recrystallization process, LAGBs are constantly transformed into HAGBs, which are gradually extended into coarse grains, and the size of coarse grains is reduced.

The flow stress is influenced by the combination of subgrains dislocation density and proportion of recrystallization. Compared to constant strain rates, the subgrains dislocation density is the smallest under the variable strain rate condition, which suggests that the alloy undergoes more efficient dynamic recovery and recrystallization processes. Although the difference in recrystallization dislocation density between the low strain rate of constant 1 s^{-1} and variable strain rate is not significant, the proportion of recrystallization grains is the largest and the proportion of subgrains is the smallest under the variable strain rate, resulting in the lower peak flow stress due to fuller recrystallization during deformation.

4.2 Effect of Variable Strain Rate Compression on Slip Deformation

For the purpose of investigating the effect of variable strain rate on types of slip deformation, and comparing it with constant strain rate conditions, the proportion of each slip type in as-extrude initial alloy, and the alloy after compression under different strain rates was statistically determined in conjunction with the SFs.
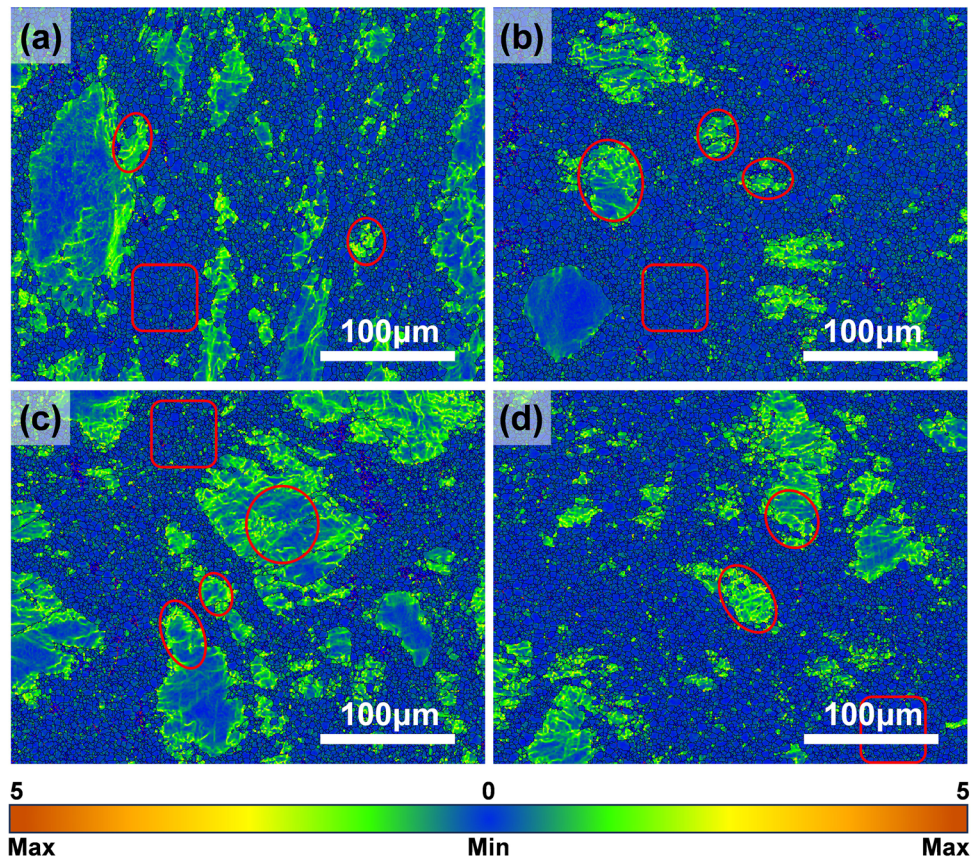
Fig. 8 Kernel Average Misorientation (KAM) distribution of the alloy under different conditions. (a) Initial, (b) variable strain rate, (c) constant 1 s^{-1}, (d) constant 10 s^{-1}

Table 2 The GND values of different grain regions under different conditions

| Strain rate of deformation	Whole grain region, m^{-2}	Recrystallization grain region, m^{-2}	Subgrain region, m^{-2}	$\rho_m^{\,3}/\dot{\varepsilon}$
Initial	5.6×10^{13}	3.2×10^{13}	2.3×10^{14}	None
1 s^{-1}	5.8×10^{13}	3.4×10^{13}	2.4×10^{14}	1.38×10^{43}
10 s^{-1}	4.9×10^{13}	2.9×10^{13}	3.5×10^{14}	4.29×10^{42}
1_10 s^{-1}	4.5×10^{13}	3.3×10^{13}	1.9×10^{14}	$6.85 \times 10^{41\sim42}$

Figure 10(a) shows the grain proportion of four main slip types in the Mg-9Gd-4Y-1Zn-0.5Zr alloy under different deformation conditions. For different deformation states, the basal slip and prismatic slip are more predominant, the pyramidal $<a>$ slip is the least, and the pyramidal $<c + a>$ slip increases sequentially with an increasing strain rate. The as-extruded initial alloy has 29% of basal slip, 56% of prismatic slip, 5% of pyramidal $<a>$ slip and 10% of pyramidal $<c + a>$ slip. The percentage of basal slip increases after compressed, but the percentage remains almost the same. However, the proportion of prismatic slip decreases to different degrees.

When deformed under constant 1 s^{-1} strain rate and variable strain rate, the proportion of prismatic slip is 46% and 43%, and that is the smallest with 32% under the strain rate of constant 10 s^{-1}, which are reduced by 10%, 13% and 24% compared with the initial alloy. The reduction of prismatic slip proportion is close to same under the first two strain rate conditions, and the maximum reduction of prismatic slip is observed under strain rate of constant 10 s^{-1}, as shown in Fig. 10(b). After the alloy is compressed, the pyramidal $<a>$ slip remains essentially the same as the initial alloy. For pyramidal $<c + a>$ slip, the proportion of initial alloy under the strain rate of constant 1 s^{-1} is low with 11% and 16% under the variable strain rate, the highest with 24% under a strain rate of constant 10 s^{-1}. Compared to the 10% of initial, pyramidal $<c + a>$ slip increased by 14% under the strain rate of constant 10 s^{-1}, 1% under strain rate of constant 1 s^{-1}, and 6% under the variable strain rate. There is the proportion change of pyramidal $<c + a>$ slip under the change strain rate between the constant low and high strain rates.

The mainly slip deformation types are basal slip and prismatic slip in the initial alloy, but the proportion of prismatic slip is greatly reduced after compression. The slip type changes from prismatic slip to basal slip and pyramidal $<c + a>$ slip. However, it is not much different regarding the change of
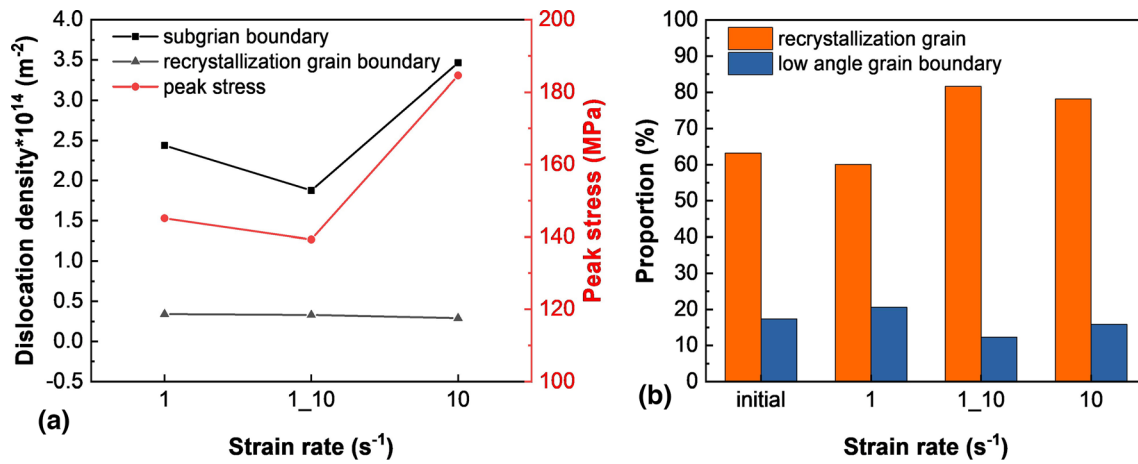
Fig. 9 The relationship among dislocation density, recrystallization and flow stress. (a) Dislocation density and peak flow stress, (b) low-angle grain boundary (LAGB) and recrystallization
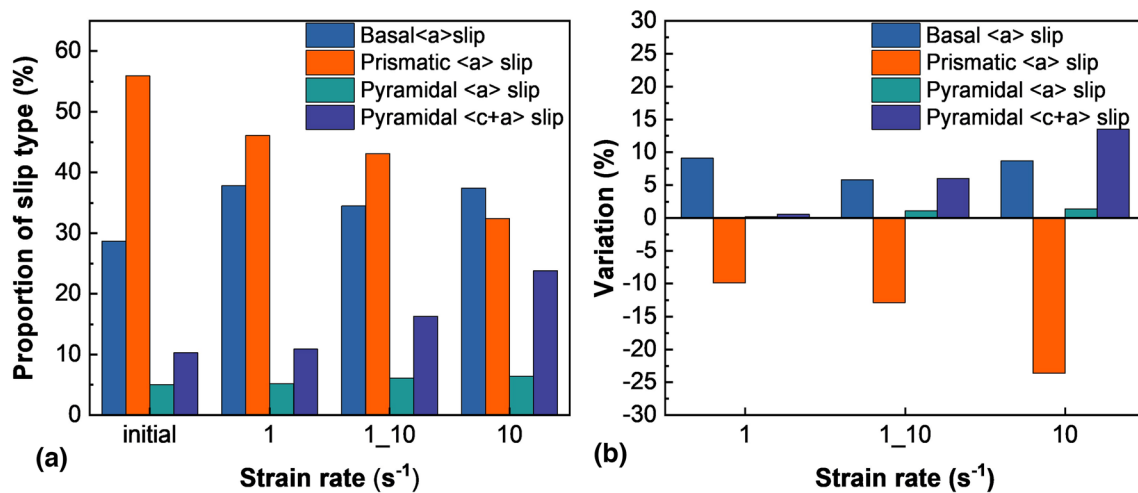
Fig. 10 Statistics of identified slip types under different conditions. (a) The proportion of slip types, (b) the variation of slip types after compressed

basal $<a>$ slip under different strain rate conditions, and the slip type importantly changes from prismatic slip to pyramidal $<c + a>$ slip. More and more prismatic slip is transformed to pyramidal $<c + a>$ leading to the increase in the CRSS during slip deformation with the increasing strain rate. The proportion change in pyramidal $<c + a>$ slip under the change strain rate condition is between the constant low and high strain rates. Therefore, the steady-state flow stress under variable strain rate condition is smaller than that under the strain rate of constant 10 s^{-1}, and higher than that under the strain rate of constant 1 s^{-1}.

5. Conclusions

The hot deformation flow behavior and microstructures of as-extruded Mg-9Gd-4Y-1Zn-0.5Zr alloy with a low strain rate of constant 1 s^{-1}, high strain rate of constant 10 s^{-1} and variable strain rate from 1 s^{-1} to 10 s^{-1} were studied. Significant conclusions are drawn as follows:

(1) The sudden increase in strain rate brings about an increase in flow stress. The peak flow stress is 142 MPa when deformed under variable strain rate from 1 s^{-1} to 10 s^{-1}, approaching the peak value of 146 MPa under the strain rate of constant 1 s^{-1} and smaller than that of 187 MPa under the strain rate of constant 10 s^{-1}. As strain proceeds, the steady-state flow stress of variable strain rate deformation is intermediate between low strain rate and high strain rate.

(2) Flow stress is related to subgrain dislocation density and proportion of recrystallization. Under the variable strain rate, the largest recrystallization area proportion of 81.6% and the smallest LAGBs proportion of 12.3% are observed. The lowest dislocation density and the smallest proportion of subgrains lead to the smallest peak flow stress.

(3) Deformation under different strain rates activates four slip systems. The slip deformation type mainly changes from prismatic $<a>$ slip to pyramidal $<c + a>$ slip. When compressed under variable strain rate, the moderate proportion change of pyramidal $<c + a>$ slip with the highest CRSS results in the steady-state flow stress

is lower than that under strain rate of constant 10 s^{-1}, and higher than that under strain rate of constant 1 s^{-1}.

Acknowledgments

Authors Contribution

ZL contributed to investigation, data curation, formal analysis, visualization, writing—original draft, and writing—review and editing. XG was involved in supervision, funding acquisition, methodology, project administration and writing—review and editing. LY contributed to methodology and investigation. CT was involved in methodology and conceptualization. YW contributed to methodology, conceptualization and formal analysis. YD was involved in methodology and conceptualization.

Competing interests

The authors declare that they have no known competing financial interests or personal relationships that could have appeared to influence the work reported in this paper.

References

1. Y. Yang, X.M. Xiong, J. Chen, X. Peng, D. Chen, and F. Pan, Research Advances of Magnesium and Magnesium Alloys Worldwide in 2022, *J. Magnes. Alloy*, 2023, **11**(8), p 2611–2654. https://doi.org/10.1016/j.jma.2023.07.011

2. T. Chen, Z. Chen, J. Shao, R. Wang, L. Mao, and C. Liu, The Role of Long-Period Stacking Ordered Phases in the Deformation Behavior of a Strong Textured Mg-Zn-Gd-Y-Zr Alloy Sheet Processed by Hot Extrusion, *Mater. Sci. Eng. A*, 2019, **750**, p 31–39. https://doi.org/10.1016/j.msea.2019.02.040

3. H. Shi, Y. Huang, Q. Luo, S. Gavras, R. Willumeit-Römer, and N. Hort, A Short Review on Diffusion Coefficients in Magnesium Alloys and Related Applications, *J. Magnes. Alloy*, 2022, **10**(12), p 3289–3305. https://doi.org/10.1016/j.jma.2022.12.003

4. J. Song, J. She, D. Chen, and F. Pan, Latest Research Advances on Magnesium and Magnesium Alloys Worldwide, *J. Magnes. Alloy*, 2020, **8**(1), p 1–41. https://doi.org/10.1016/j.jma.2020.02.003

5. J. Jiang, H. Xu, Y. Wang, G. Bi, Y. Li, and T. Chen, Deformation Behavior, Microstructure Evolution and Hot Workability of an Extruded Mg-2Y-0.5Zn-0.5Ni Alloy, *J. Mater. Eng. Perform.*, 2024, **33**(6), p 2749–2808. https://doi.org/10.1007/s11665-023-08158-z

6. S.R. Agnew and Ö. Duygulu, Plastic Anisotropy and the Role of Non-basal Slip in Magnesium Alloy AZ31B, *Int. J. Plast.*, 2005, **21**(6), p 1161–1193. https://doi.org/10.1016/j.ijplas.2004.05.018

7. K. Zhang and J. Jiang, Effects of Grain Size and Temperature on Slip and Twinning Activity in a Magnesium-Rare Earth Alloy, *Mater. Sci. Eng. A*, 2024, **891**, p 145974. https://doi.org/10.1016/j.msea.2023.145974

8. W.T. Sun, X.G. Qiao, M.Y. Zheng, C. Xu, S. Kamado, X.J. Zhao, H.W. Chen, N. Gao, and M.J. Starink, Altered Ageing Behavior of a Nanostructured Mg-8.2Gd-3.8Y-1.0Zn-0.4Zr Alloy Processed by High Pressure Torsion, *Acta Mater.*, 2018, **151**, p 260–270. https://doi.org/10.1016/j.actamat.2018.04.003

9. H. Wang, X. Sun, S. Kurukuri, M.J. Worswick, D.Y. Li, Y.H. Peng, and P.D. Wu, The Strain Rate Sensitive and Anisotropic Behavior of Rare-Earth Magnesium Alloy ZEK100 Sheet, *J. Magnes. Alloy*, 2023, **11**(3), p 882–891. https://doi.org/10.1016/j.jma.2021.06.010

10. P. Bai, J. Wang, Z. Zhao, W. Du, D. Tie, C. Cai, R. Zhang, and F. Wang, Microstructure and Mechanical Properties of Mg-Gd-Y-Zn-Zr Alloy Fabricated by Cold Metal Transfer Wire Arc Additive Manufacturing, *J. Mater. Res. Technol.*, 2023, **27**, p 5805–5821. https://doi.org/10.1016/j.jmrt.2023.10.265

11. H.T. Jeong and W.J. Kim, The Hot Compressive Deformation Behavior of Cast Mg-Gd-Y-Zn-Zr Alloys With and Without LPSO Phase in their Initial Microstructures, *J. Magnes. Alloy*, 2022, **10**(10), p 2901–2917. https://doi.org/10.1016/j.jma.2022.01.006

12. G. Wu, C. Wang, M. Sun, and W. Ding, Recent Developments and Applications on High-Performance Cast Magnesium Rare-Earth Alloys, *J. Magnes. Alloy*, 2021, **9**(1), p 1–20. https://doi.org/10.1016/j.jma.2020.06.021

13. J. Wang, Z. Zhao, W. Du, P. Bai, L. Wang, Z. Zhang, and Z. Huang, High-Temperature Compression Deformation Strengthening Mechanism of Mg-Gd-Y-Zn-Zr Alloy Formed by Cold Metal Transfer (CMT) Arc Additive Forming, *Mater. Sci. Eng. A*, 2024, **893**, p 146084. https://doi.org/10.1016/j.msea.2024.146084

14. X. Xia, Q. Chen, J. Li, D. Shu, C. Hu, S. Huang, and Z. Zhao, Characterization of Hot Deformation Behavior of As-extruded Mg-Gd-Y-Zn-Zr Alloy, *J. Alloys Compd.*, 2014, **610**, p 203–211. https://doi.org/10.1016/j.jallcom.2014.04.210

15. L. Li, Y. Wang, C. Zhang, T. Wang, H. Lv, and W. Yu, Ultrafine-grained Mg-Zn-Yb-Zr Alloy with Simultaneously Improved Strength and Ductility Processed by Axisymmetric Hot Extrusion, *Vacuum*, 2020, **173**, p 109157. https://doi.org/10.1016/j.vacuum.2019.109157

16. Y. Huang, G. Zeng, L. Huang, Z. Zheng, C. Liu, and H. Zhan, Influence of Strain Rate on Dynamic Recrystallization Behavior and Hot Formability of Basal-textured AZ80 Magnesium Alloy, *Mater Charact*, 2022, **187**, p 111880. https://doi.org/10.1016/j.matchar.2022.111880

17. J. Li, F. Wang, J. Zeng, C. Zhao, L. Jin, and J. Dong, Effect of the Interspacing of Intragranular Lamellar LPSO Phase on Dynamic Recrystallization Behaviors of Mg-Gd-Y-Zn-Zr Alloys, *Mater Charact*, 2022, **193**, p 112326. https://doi.org/10.1016/j.matchar.2022.112326

18. L. Jia, J. Zheng, Z. Yan, L. Liu, X. Dai, Z. Zhang, and Y. Xue, Effect of Pre-aging on Microstructure, Activation Energy, Texture Evolution of Mg-9Gd-4Y-2Zn-0.5Zr Alloy During Compression Deformation, *J. Mater. Res. Technol.*, 2023, **26**, p 4755–4769. https://doi.org/10.1016/j.jmrt.2023.08.201

19. X. Yang, B. Liu, X. Zhou, W. Huang, L. Lu, X. Lu, and Y. Liu, Hot Compression Behavior and Workability of Mg-5Gd-3Y-2Zn-0.5Zr Alloy with Long-Period Stacking Ordered Phases, *J. Mater. Eng. Perform.*, 2023, **32**(5), p 2041–2049. https://doi.org/10.1007/s11665-022-07256-8

20. W. Xu, J. Yu, L. Jia, G. Wu, and Z. Zhang, Deformation Behavior of Mg-13Gd-4Y-2Zn-0.5Zr Alloy on the Basis of LPSO Kinking, Dynamic Recrystallization and Twinning During Compression-Torsion, *Mater Charact*, 2021, **178**, p 111215. https://doi.org/10.1016/j.matchar.2021.111215

21. L. Hu, M. Lang, L. Shi, M. Li, T. Zhou, C. Bao, and M. Yang, Study on Hot Deformation Behavior of Homogenized Mg-8.5Gd-4.5Y-0.8Zn-0.4Zr Alloy Using a Combination of Strain-Compensated Arrhenius Constitutive Model and Finite Element Simulation Method, *J. Magnes. Alloy*, 2023, **11**(3), p 1016–1028. https://doi.org/10.1016/j.jma.2021.07.008

22. T. Sakai, A. Belyakov, R. Kaibyshev, H. Miura, and J.J. Jonas, Dynamic and Post-Dynamic Recrystallization under Hot, Cold and Severe Plastic Deformation Conditions, *Prog. Mater. Sci.*, 2014, **60**, p 130–207. https://doi.org/10.1016/j.pmatsci.2013.09.002

23. M.F. Abbod, C.M. Sellars, A. Tanaka, D.A. Linkens, and M. Mahfouf, Effect of Changing Strain Rate on Flow Stress during Hot Deformation of Type 316L Stainless Steel, *Mater. Sci. Eng. A*, 2008, **491**(1–2), p 290–296. https://doi.org/10.1016/j.msea.2008.02.005

24. Y.X. Liu, Z.J. Ke, and R.H. Li, Effects of Sudden Changes in Strain Rate on Hot Deformation Behavior of Inconel 718, *Mater. Today Commun.*, 2023, **34**, p 105295. https://doi.org/10.1016/j.mtcomm.2022.105295

25. C. Zhang, Y. Du, L. Zhang, C. Jin, X. Zhou, and F. Li, Hot Deformation Behavior of C276 Superalloy in Shifted Strain Rate Compression: Experiments and Cellular Automaton Modelling, *J. Alloys Compd.*, 2022, **898**, p 162775. https://doi.org/10.1016/j.jallcom.2021.162775

26. M.S. Chen, Z.H. Zou, Y.C. Lin, and K.K. Li, Hot Deformation Behaviors of a Solution-Treated Ni-Based Superalloy Under Constant and Changed Strain Rates, *Vacuum*, 2018, **155**, p 531–538. https://doi.org/10.1016/j.vacuum.2018.06.059

27. K. Huang and R.E. Logé, Microstructure and Flow Stress Evolution During Hot Deformation of 304L Austenitic Stainless Steel in Variable Thermomechanical Conditions, *Mater. Sci. Eng. A*, 2018, **711**, p 600–610. https://doi.org/10.1016/j.msea.2017.11.042

28. Q. Li, H. Yan, H. Liu, and R. Chen, Dynamic Recrystallization Mechanism and Near-Isotropic Mechanical Properties of WE43 Magnesium Alloy Sheets Rolled at Different Temperatures, *Mater Charact*, 2022, **193**, p 112259. https://doi.org/10.1016/j.matchar.2022.112259

29. S.M. Fatemi and H. Paul, Characterization of Continuous Dynamic Recrystallization in WE43 Magnesium Alloy, *Mater. Chem. Phys.*, 2021, **257**, p 123726. https://doi.org/10.1016/j.matchemphys.2020.123726

30. S. Wang, W. Zhang, J. Yang, J. Pan, H. Wang, W. Chen, and G. Cui, Evolution of Microstructures, Texture, Damping and Mechanical Properties of Hot Extruded Mg-Nd-Zn-Zr Alloy, *J. Mater. Eng. Perform.*, 2021, **30**(12), p 8872–8882. https://doi.org/10.1007/s11665-021-06134-z

31. A. Imandoust, C.D. Barrett, A.L. Oppedal, W.R. Whittington, Y. Paudel, and H. El Kadiri, Nucleation and Preferential Growth Mechanism of Recrystallization Texture in High Purity Binary Magnesium-Rare Earth Alloys, *Acta Mater.*, 2017, **138**, p 27–41. https://doi.org/10.1016/j.actamat.2017.07.038

32. Y. Wu, Y. Jia, S. Zhang, Y. Liu, H. Xiong, and G. Chen, Flow Softening and Dynamic Recrystallization Behavior of a Mg-Gd-Y-Nd-Zr Alloy under Elevated Temperature Compressions, *J. Magnes. Alloy*, 2023, **11**(8), p 2891–2900. https://doi.org/10.1016/j.jma.2021.11.009

33. H. Mirzadeh, Grain Refinement of Magnesium Alloys by Dynamic Recrystallization (DRX): A Review, *J. Mater. Res. Technol.*, 2023, **25**, p 7050–7077. https://doi.org/10.1016/j.jmrt.2023.07.150

34. Q. Qin, Y. Tan, Z. Zhang, Q. Wang, and Y. Yang, Effects of Homogenization on Hot Deformation Behavior of As-Cast Mg-8Gd-3Y-1Nd-0.5Zr Magnesium Alloy, *J. Mater. Eng. Perform.*, 2016, **25**(1), p 304–311. https://doi.org/10.1007/s11665-015-1807-4

35. Q. Chen, L. Hu, M. Li, Y. Chen, L. Shi, T. Zhuo, and M. Yang, Optimizing Process Parameters of As-Homogenized Mg-Gd-Y-Zn-Zr Alloy in Isothermal Uniaxial Compression on the Basis of Processing Maps via Prasad Criterion and Murty Criterion, *J. Mater. Eng. Perform.*, 2022, **31**(3), p 2257–2266. https://doi.org/10.1007/s11665-021-06305-y

36. P. Prakash, J. Uramowski, M.A. Wells, and B.W. Williams, Influence of Initial Microstructure on the Hot Deformation Behavior of AZ80 Magnesium Alloy, *J. Mater. Eng. Perform.*, 2023, **32**(6), p 2647–2660. https://doi.org/10.1007/s11665-022-07151-2

37. C. Tang, J. Chen, X. Ma, W. Liu, H. Xie, M. Li, and X. Liu, Effects of Extrusion Speed on the Formation of Bimodal-Grained Structure and Mechanical Properties of a Mg-Gd-Based Alloy, *Mater Charact*, 2022, **189**, p 111952. https://doi.org/10.1016/j.matchar.2022.111952

38. X. Lu, G. Zhao, J. Zhou, C. Zhang, and L. Sun, Effect of Extrusion Speeds on the Microstructure, Texture and Mechanical Properties of High-Speed Extrudable Mg-Zn-Sn-Mn-Ca Alloy, *Vacuum*, 2018, **157**, p 180–191. https://doi.org/10.1016/j.vacuum.2018.08.041

39. Y. Du, B. Jiang, and Y. Ge, Effects of Precipitates on Microstructure Evolution and Texture in Mg-Zn alloy during Hot Deformation, *Vacuum*, 2018, **148**, p 27–32. https://doi.org/10.1016/j.vacuum.2017.11.002

40. L. Chen, M. Liang, G. Zhao, J. Zhou, and C. Zhang, Microstructure Evolution of AZ91 Alloy During Hot Extrusion Process with Various Ram Velocity, *Vacuum*, 2018, **150**, p 136–143. https://doi.org/10.1016/j.vacuum.2018.01.036

41. P. Kot, M. Wroński, A. Baczmański, A. Ludwik, S. Wroński, K. Wierzbanowski, Ch. Scheffzük, J. Pilch, and G. Farkas, A Novel Method of Experimental Determination of Grain Stresses and Critical Resolved Shear Stresses for Slip and Twin Systems in a Magnesium Alloy, *Measurement*, 2023, **221**, p 113469. https://doi.org/10.1016/j.measurement.2023.113469

42. G. Wang, P. Mao, Z. Wang, L. Zhou, F. Wang, and Z. Liu, High Strain Rates Deformation Behavior of an As-Extruded Mg-2.5Zn-4Y Magnesium Alloy Containing LPSO Phase at High Temperatures, *J. Mater. Res. Technol.*, 2022, **21**, p 40–53. https://doi.org/10.1016/j.jmrt.2022.08.131

43. K. Huang and R.E. Logé, A Review of Dynamic Recrystallization Phenomena in Metallic Materials, *Mater. Des.*, 2016, **111**, p 548–574. https://doi.org/10.1016/j.matdes.2016.09.012

44. M.S. Chen, W.Q. Yuan, H.B. Li, and Z.H. Zou, New Insights on the Relationship Between Flow Stress Softening and Dynamic Recrystallization Behavior of Magnesium Alloy AZ31B, *Mater Charact*, 2019, **147**, p 173–183. https://doi.org/10.1016/j.matchar.2018.10.031

45. F. Nazeer, S.Z. Hassan Naqvi, A. Kalam, A.G. Al-Sehemi, and H. Alrobei, Texture Dependencies on Flow Stress Behavior of Magnesium Alloy Under Dynamic Compressive Loading, *Vacuum*, 2021, **191**, p 110323. https://doi.org/10.1016/j.vacuum.2021.110323

46. J. Jia, H. Zhang, M. Meng, X. Yang, X. Zhang, and Z. Zhang, Strain-Induced Heterogeneous Bimodal Microstructure Behavior of Mg-Gd-Y-Zn-Zr Alloy Containing LPSO Phase During Hot Compression, *J. Mater. Res. Technol.*, 2023, **27**, p 4264–4277. https://doi.org/10.1016/j.jmrt.2023.10.262

47. M. Calcagnotto, D. Ponge, E. Demir, and D. Raabe, Orientation Gradients and Geometrically Necessary Dislocations in Ultrafine Grained Dual-Phase Steels Studied by 2D and 3D EBSD, *Mater. Sci. Eng. A*, 2010, **527**, p 2738–2746. https://doi.org/10.1016/j.msea.2010.01.004

48. X. Zhou, Y. Yao, J. Zhang, X. Chen, W. Huang, J. Pan, H. Wang, and M. Weng, A High-Performance Mg-4.9Gd-3.2Y-1.1Zn-0.5Zr Alloy Via Multidirectional Forging After Analyzing Its Compression Behavior, *J. Mater. Res. Technol.*, 2021, **70**, p 156–167. https://doi.org/10.1016/j.jmst.2020.08.054

49. M.A. Lopez-Sanchez, A. Tommasi, F. Barou, and R. Quey, Dislocation-Driven Recrystallization in AZ31B Magnesium Alloy Imaged by Quasi-In Situ EBSD in Annealing Experiments, *Mater Charact*, 2020, **165**, p 110382. https://doi.org/10.1016/j.matchar.2020.110382